

## Comparison of velocimetry techniques for turbulent structures in gas-puff imaging data

J. M. Sierchio, I. Cziegler, J. L. Terry, A. E. White, and S. J. Zweben

Citation: [Review of Scientific Instruments](#) **87**, 023502 (2016); doi: 10.1063/1.4939672

View online: <http://dx.doi.org/10.1063/1.4939672>

View Table of Contents: <http://scitation.aip.org/content/aip/journal/rsi/87/2?ver=pdfcov>

Published by the [AIP Publishing](#)

---

### Articles you may be interested in

[Dynamical programming based turbulence velocimetry for fast visible imaging of tokamak plasma](#)  
Rev. Sci. Instrum. **86**, 033505 (2015); 10.1063/1.4914838

[Development of the gas-puff imaging diagnostic in the TEXTOR tokamak](#)  
Rev. Sci. Instrum. **84**, 053501 (2013); 10.1063/1.4803934

[New dual gas puff imaging system with up-down symmetry on experimental advanced superconducting tokamak](#)  
Rev. Sci. Instrum. **83**, 123506 (2012); 10.1063/1.4770122

[Comparison of scrape-off layer turbulence simulations with experiments using a synthetic gas puff imaging diagnostic](#)  
Phys. Plasmas **18**, 022306 (2011); 10.1063/1.3553024

[Edge turbulence measurements in NSTX by gas puff imaging](#)  
Rev. Sci. Instrum. **72**, 931 (2001); 10.1063/1.1321009

---



# Comparison of velocimetry techniques for turbulent structures in gas-puff imaging data

J. M. Sierchio,<sup>1,a)</sup> I. Cziegler,<sup>2</sup> J. L. Terry,<sup>1</sup> A. E. White,<sup>1</sup> and S. J. Zweben<sup>3</sup>

<sup>1</sup>Plasma Science and Fusion Center, Massachusetts Institute of Technology, Cambridge, Massachusetts 02139, USA

<sup>2</sup>Center for Momentum Transport and Flow Organization, University of California, San Diego, La Jolla, California 92093, USA

<sup>3</sup>Princeton Plasma Physics Laboratory, Princeton, New Jersey 08543, USA

(Received 1 July 2015; accepted 26 December 2015; published online 2 February 2016)

Recent analysis of Gas Puff Imaging (GPI) data from Alcator C-Mod found blob velocities with a modified tracking time delay estimation (TDE). These results disagree with velocity analysis performed using direct Fourier methods. In this paper, the two analysis methods are compared. The implementations of these methods are explained, and direct comparisons using the same GPI data sets are presented to highlight the discrepancies in measured velocities. In order to understand the discrepancies, we present a code that generates synthetic sequences of images that mimic features of the experimental GPI images, with user-specified input values for structure (blob) size and velocity. This allows quantitative comparison of the TDE and Fourier analysis methods, which reveals their strengths and weaknesses. We found that the methods agree for structures of any size as long as all structures move at the same velocity and disagree when there is significant nonlinear dispersion or when structures appear to move in opposite directions. Direct Fourier methods used to extract poloidal velocities give incorrect results when there is a significant radial velocity component and are subject to the barber pole effect. Tracking TDE techniques give incorrect velocity measurements when there are features moving at significantly different speeds or in different directions within the same field of view. Finally, we discuss the limitations and appropriate use of each of methods and applications to the relationship between blob size and velocity. © 2016 AIP Publishing LLC. [<http://dx.doi.org/10.1063/1.4939672>]

## I. INTRODUCTION

Turbulence is one the major issues currently preventing the realization of fusion as a viable energy source. It is the primary cause of plasma transport across the confining magnetic field lines, resulting in loss of plasma heat and particles, poor plasma confinement,<sup>1</sup> and plasma-wall interactions. Because this is such an important problem, we are interested in all properties of the turbulent structures in the plasma: their dynamics (momentum), their density and temperature fluctuation magnitudes, and their length scales. Physically, the fluctuations typical of scrape-off layer (SOL) turbulence<sup>2</sup> can be characterized as filaments along magnetic field lines, while appearing to have some structure perpendicular to the field lines. These filament structures are usually referred to as blobs.<sup>3–5</sup>

Multiple diagnostic systems are in use to study plasma turbulence, including probes and beam emission spectroscopy.<sup>6–9</sup> One of the most successful diagnostics to study SOL turbulence is gas-puff imaging (GPI), a technique which is based on imaging the line radiation emitted by a locally puffed neutral gas such as deuterium or helium, as its atoms are excited by the edge plasma.<sup>3,10</sup> There are GPI diagnostic systems currently installed on Alcator C-Mod,<sup>11</sup> NSTX,<sup>12</sup> EAST,<sup>13</sup> and TEXTOR.<sup>14</sup> The light signals can be used to mea-

sure properties of the turbulence such as density fluctuations,<sup>15</sup> or derived quantities such as structure velocities. The general use of velocimetry, and studying turbulent structure velocities, in particular, is important for edge transport and plasma flux,<sup>16</sup> shear,<sup>17,18</sup> and time-dependent analysis. The GPI diagnostic technique has been used in a number of different studies, including blob dynamics,<sup>18–20</sup> zonal flows and geodesic-acoustic modes,<sup>21–23</sup> coherent electrostatic modes,<sup>24</sup> and code validation.<sup>25</sup>

This paper uses data from Alcator C-Mod only. On C-Mod, there are two GPI systems that view the same volume emission from the same gas puff. One system detects the emission with the  $64 \times 64$  pixel array of a Phantom 710 fast-framing camera, covering a  $\sim 6 \text{ cm} \times 6 \text{ cm}$  view of the puff, giving a Nyquist limit in poloidal wavenumber of  $33 \text{ cm}^{-1}$ ; the other detects emission using a  $9 \times 10$  array of fibers that are routed to avalanche photodiodes (APDs), covering a  $\sim 3.4 \text{ cm} \times 3.7 \text{ cm}$  view of the puff, giving a Nyquist limit of  $8.1 \text{ cm}^{-1}$ .<sup>15,26</sup> In this paper we will refer to the two systems as the “Phantom-based” and “APD-based” and use data almost exclusively from the Phantom-based system. The Phantom-based system includes telescope optics and a fine optic bundle; the total spatial resolution is  $\sim 2\text{--}3 \text{ mm}$ .<sup>19</sup> The APDs view the gas puff purely toroidally, while the camera views the puff at an  $11^\circ$  angle below horizontal, along the local magnetic field.

Several different methods for velocity analysis of GPI data have been described in the literature. Some measure

<sup>a)</sup>sierchio@mit.edu

speeds in one spatial dimension, others in two spatial dimensions, depending on whether the data sets are arrays of one spatial dimension versus 2D images. Some of the methods include optical flow or pattern tracking techniques which find local velocity fields which map one image to the next,<sup>16,27,28</sup> time-delay estimation (TDE) with either wavelets and cross correlations,<sup>19,23</sup> and direct Fourier analysis (FA) which finds a wavenumber-frequency spectrum and thus a phase velocity.<sup>15,29,30</sup> We will not attempt to treat the exhaustive list of techniques but rather focus on specific implementations (codes) whose results have been examined in detail and have been used in the literature recently for C-Mod data.<sup>15,19</sup>

In the work presented here, we examine modified tracking TDE (tracking TDE)<sup>19</sup> and direct FA<sup>15,26</sup> methods, with analysis both in time and one spatial dimension. The motivation for this is that when direct FA is applied to the same C-Mod shots analyzed by Zweben *et al.*<sup>19</sup> using tracking TDE, the results do not agree in many cases with those obtained using tracking TDE. In this paper, we investigate these two analysis techniques in order to (1) demonstrate cases when they agree and when they do not, and (2) for those cases in which they do not agree, understand the reasons why.

The paper is organized as follows. Section II presents some initial GPI data and results for the two techniques. Section III describes the techniques and implementations in detail. Section IV presents further tests of the strengths and weaknesses of each method, through the use of synthetic data. Section V describes the strengths and weaknesses of each method as discovered through analyzing the synthetic data. Section VI discusses some new physics revealed during these tests, pertaining to multiple velocity measurements and size scales. Section VII explains a number of caveats and cautions in interpreting our results, along with making comments about the appropriate use of each method. And finally, Section VIII concludes the paper.

## II. DESCRIPTION OF TECHNIQUES

As mentioned above, we are comparing a direct FA technique to a tracking TDE method. In general, direct FA methods will be mathematically equivalent to TDE methods through the correlation theorem,<sup>31</sup> which states that the Fourier transform of the cross correlation of two function is simply the Fourier transform of the first function multiplied by the Fourier transform of the complex conjugate of the second function. Here, we briefly describe in this section how each method is practically implemented in the analysis codes.

### A. Velocimetry using Fourier analysis

The general idea behind the Fourier analysis technique is to break up a time signal into its temporal and spatial Fourier components and then to evaluate the phase velocity  $V_{ph} = \omega/k$  as the line passing through the largest magnitude Fourier components as a function of wavenumber  $k$  and frequency  $\omega$ .<sup>15,26,29,30,32</sup>

The numerical Fourier analysis gives the wavenumber-frequency spectrum,  $S(k, \omega)$ , for a signal time-series from a

linear array of spatially separated locations, where  $k$  is the wavenumber of features projected along the array. All spatial locations are included when computing the spectrum. Since for the velocity analysis we generally choose to give equal weight to all frequencies, we normalize the spectral density at each frequency, giving the conditional spectrum<sup>30</sup>

$$s(k|\omega) = \frac{S(k, \omega)}{S(\omega)}, \quad (1)$$

where  $s(k|\omega)$  is the conditional spectral density,  $S(k, \omega)$  is the spectral density as a function of both wavenumber and frequency, and  $S(\omega)$  is the spectral density integrated over the wavenumbers at each frequency. Any artifacts or aliasing in the high- $k$  power spectrum can be mitigated by applying a correction factor; this correction was applied for all conditional spectra in this paper. An example of a conditional spectrum from the Phantom-based GPI for a C-Mod shot is shown in Fig. 1; the phase velocity was found to be  $3.1 \pm 0.3$  km/s, fitting the peak in the Fourier spectrum at 30 kHz. For instances in which low frequency flows are important, the velocity analysis can be completed by using the wavenumber-frequency spectrum without normalizing. We have compared velocity results using both the normalized (conditional) and un-normalized spectra for several shots; differences were found to be typically less than 10% and no more than 15%.

We consider the plasma turbulence to have linear dispersion when both the derivative of  $\omega$  with respect to  $k$  is a constant and  $\omega(k = 0) = 0$ . When this occurs, the group and phase velocities are equal. In implementing this technique, the analysis could be attempted by first assuming linear dispersion, and thus taking the phase velocity to be the slope along the maxima in the wavenumber-frequency spectrum. If non-linear dispersion is present, the group velocity may be found by fitting a function to the peaks in the spectra and taking the derivative.

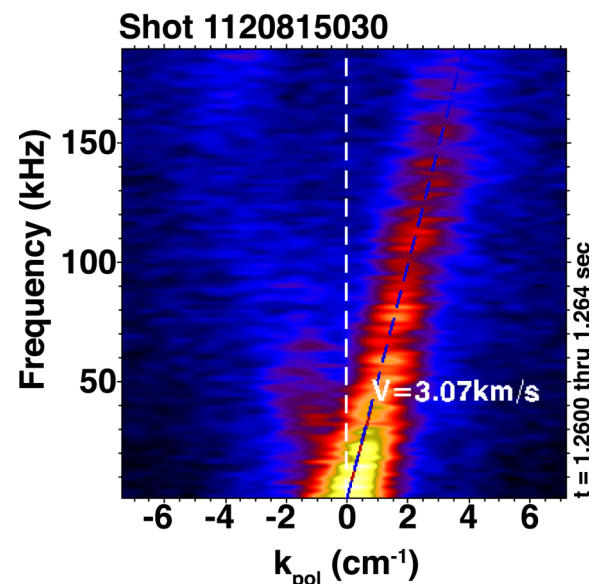


FIG. 1. Direct Fourier Analysis conditional spectrum from Phantom-based GPI data for C-Mod shot #1120815030, at 2.05 cm outside the separatrix. The poloidal phase velocity was found to be  $3.1 \pm 0.3$  km/s.

As mentioned above, the GPI data are three-dimensional in that there are two spatial dimensions and one temporal. In many implementations, the spatial Fourier transform can be taken in both spatial dimensions. However, for the specific implementation considered here, the spatial Fourier transform is not performed over both dimensions; it is performed over the poloidal direction only, giving a poloidal wavenumber. This is because the magnetic flux surfaces are approximately parallel to the vertical direction in the 2D image. The radial direction is approximately horizontal in the image. On Alcator C-Mod, the separatrix is usually within the field of view of the GPI detectors. If the spatial transform were to be performed over the radial direction as well, it would be performed crossing flux surfaces. This is quite problematic since the observed radial propagation inside and outside the separatrix can be quite different. One way to avoid this issue for views outside the separatrix is to perform the Fourier transform in the radial direction only outside the separatrix. However, if the radial extent is too small, i.e., there are not enough pixels over which to transform, a non-physical result will be obtained. This is indeed the case with the Fourier implementation considered here.

## B. Tracking time-delay estimation

There are several different ways to implement TDE,<sup>33</sup> and multiple codes are currently used.<sup>17,22,34,35</sup> We will focus on a modified TDE method that has been described in detail before,<sup>16,19</sup> and is summarized here. The technique uses a direct cross correlation between two discrete time signals within a predefined search box. The method has been designed for use with the GPI Phantom-based detector.<sup>19</sup> The GPI system produces a set of two-dimensional frames in time. The views/pixels each have their own sensitivities to signal, which could affect the value of the cross correlation function. Thus for any TDE method applied to GPI data it is necessary to normalize out the pixel-to-pixel variation in the response. The cross correlation function is defined for a discrete signal,

$$\frac{\sum_{k=0}^{N-|\tau|-1} (f_{k+|\tau|} - \bar{f})(g_k - \bar{g})}{\sqrt{[\sum_{k=0}^{N-1} (f_k - \bar{f})^2][\sum_{k=0}^{N-1} (g_k - \bar{g})^2]}}, \quad \tau < 0 \quad (2)$$

$$\frac{\sum_{k=0}^{N-|\tau|-1} (f_k - \bar{f})(g_{k+\tau} - \bar{g})}{\sqrt{[\sum_{k=0}^{N-1} (f_k - \bar{f})^2][\sum_{k=0}^{N-1} (g_k - \bar{g})^2]}}, \quad \tau \geq 0 \quad (3)$$

where  $N$  is the number of points in the time series of the signals  $f$  and  $g$  and  $\tau$  is the time lag.

Images taken at a 391 000 frame rate over roughly three to five milliseconds are typically analyzed. This length of time is chosen to ensure that enough data were selected to obtain an accurate answer while maintaining a reasonable time for code execution. Selecting shorter time series would result in excluding lower frequency correlations, which could be favorable or unfavorable depending on what frequency bands are of interest. In principle, a time series of any length could be used. However, selecting a long time series opens the possibility of the velocity changing during the time window; the tracking TDE method can only output one velocity measurement per

time window, so any change in velocity would not be detected. Each frame in the series is first spatially smoothed and normalized to reduce noise. Then a reference pixel is selected and a search box of  $\pm 8$  pixels in each direction surrounding it is designated, for a total of  $17 \times 17$  or 289 pixels, with a pixel viewing approximately  $1 \text{ mm} \times 1 \text{ mm}$  in the focal plane of the gas puff and with approximately 1 mm center-to-center spacing. The cross correlation function for the reference pixel and every other pixel in the search box is computed for lags up to  $\pm 10$  frames, with the time between frames being  $2.5 \mu\text{s}$ . The location at which the maximum in the cross correlation function occurs for each time lag is found, and the vector in object space divided by that time lag yields a structure velocity at the reference location for that short time series for each time lag.

To yield a final structure velocity measurement an average over velocities corresponding to the best cross correlation values is computed. For a velocity value to be used in the average, it must meet several criteria: (1) the cross correlation must be greater than a threshold of 0.5 for that time lag, (2) the peak in the cross correlation function for that time lag must be inside the search box, and (3) the peak in the cross correlation must be well-defined spatially in the sense that for the function, the peak/average ratio is greater than some user-defined threshold. Once these criteria are met for a particular time lag, the velocity local to the reference pixel is computed as the average over the velocities whose time lags meet the criteria. This process is computed for reference pixels that are not within 8 pixels of the edge of the  $64 \times 64$  pixel frame. The user has the choice of further restricting the region of reference pixels.

Because of the search box size, this particular implementation has only a range of velocities that can be detected in either the Z or the R directions, which is given as the maximum distance traveled in the time between two consecutive frames. For the chosen values of the search box size and the period between frames, this comes to 2.8 km/s in the code used. Throughout this whole process, filtering for frequencies is not applied. The resulting velocity determination is weighted towards the motion of the brightest moving features.

Once this process is completed for each pixel, a map of the pixels with their corresponding velocities can be generated, which shows the general flow of the turbulence structures both as a function of radius and Z.

This particular method has some known issues which could affect the results and are explained in detail elsewhere,<sup>16,19</sup> and we summarize them here. First, this particular implementation limits the range of velocities detectable due to the size of the search box as described above. Any flow moving faster than the cutoff described above will not be detected by this particular implementation of the tracking TDE method. Second, by the virtue of searching for the maxima in the cross correlation function and not filtering explicitly for frequency, the tracking TDE method cannot find multiple velocities at a single location, and it weights heavily the motion of the brightest moving features. At most it will find some combination of any multiple flows, so that the output should be interpreted as some average velocity in the region if, for example, these multiple flows are equally bright. The modified



tracking TDE method described here makes the assumption that the individual structures or blobs do not change in size or intensity during the selected time interval; we know in the experimental data that the measured blobs characteristics do change in time which can lead to an inaccurate measurement. This tracking method is subject to what is called the aperture effect, in which an intensity gradient is necessary to detect the motion. In other words, the tracking TDE method will fail when there is a velocity component perpendicular to the intensity gradient.

### III. DISAGREEMENT OF METHODS WHEN APPLIED TO EXPERIMENTAL DATA

The motivation behind this work is to compare two velocimetry methods when applied to the same experimental data, to understand why they may agree or disagree on a set of data, and to advise on their appropriate use. Thus, in this section, we present results of applying the FA conditional spectra and tracking TDE methods on sets of C-Mod GPI data to illustrate the types of discrepancies found. For analyses of C-Mod shots shown in Fig. 2, the red triangles represent direct FA measurements and the blue ones represent measurements made with the tracking TDE method. The time windows for the shots presented ranged from 4-15 ms, with the same time window used for both analysis techniques. Shots from 1120224 were L-modes, while 1120712027 was an Ohmic H-Mode and 1120815018 an ELMy H-Mode. Close agreement in poloidal velocity measurements was only found for one case (shot 1120224015).

There are multiple experimental examples of disagreement between the TDE and FA methods. We note several instances where the conditional spectra of direct FA show nonlinear dispersion, i.e., where the phase velocity is not constant with frequency and wavenumber. An example of this is shown in Fig. 3. In the FA conditional spectrum, we identify “lobes” as regions with large Fourier amplitudes compared to the background level. For this particular discharge and distance from the separatrix, a change in the slope of the lobes can be seen. The Fourier technique measured  $-1.44 \pm \text{km/s}$  as the velocity using a line hand-fitted to the brightest features, while the tracking TDE code measured  $-1.2 \text{ km/s}$ .

Disagreement was also found in cases where the direct FA conditional spectra show obvious lobes, one with positive wavenumbers and one with negative wavenumbers, as well as multiple lobes with the same sign in wavenumber. An example of this is given in Fig. 4. For this discharge and distance from the separatrix, the Fourier method detected two different velocities:  $-2.79 \pm 0.42 \text{ km/s}$  and  $+2.43 \pm 0.36 \text{ km/s}$  again fitting a line to the brightest features, while the tracking TDE method can only output one:  $0.1 \text{ km/s}$ .

Another example of this effect is shown in Fig. 5, in which the positive- $k$  lobe is not symmetric with the negative- $k$  lobe. The Fourier method again detected two different velocities:  $-0.93 \pm 0.14 \text{ km/s}$  and  $+1.49 \pm 0.22 \text{ km/s}$ . The tracking TDE method found roughly  $-0.6 \text{ km/s}$ .

For the shots corresponding to Figs. 4 and 5, movies of the Phantom-based GPI show that there are counter-propagating features in some columns of pixels, but necessarily the same exact location. Since the Fourier analysis computes velocity

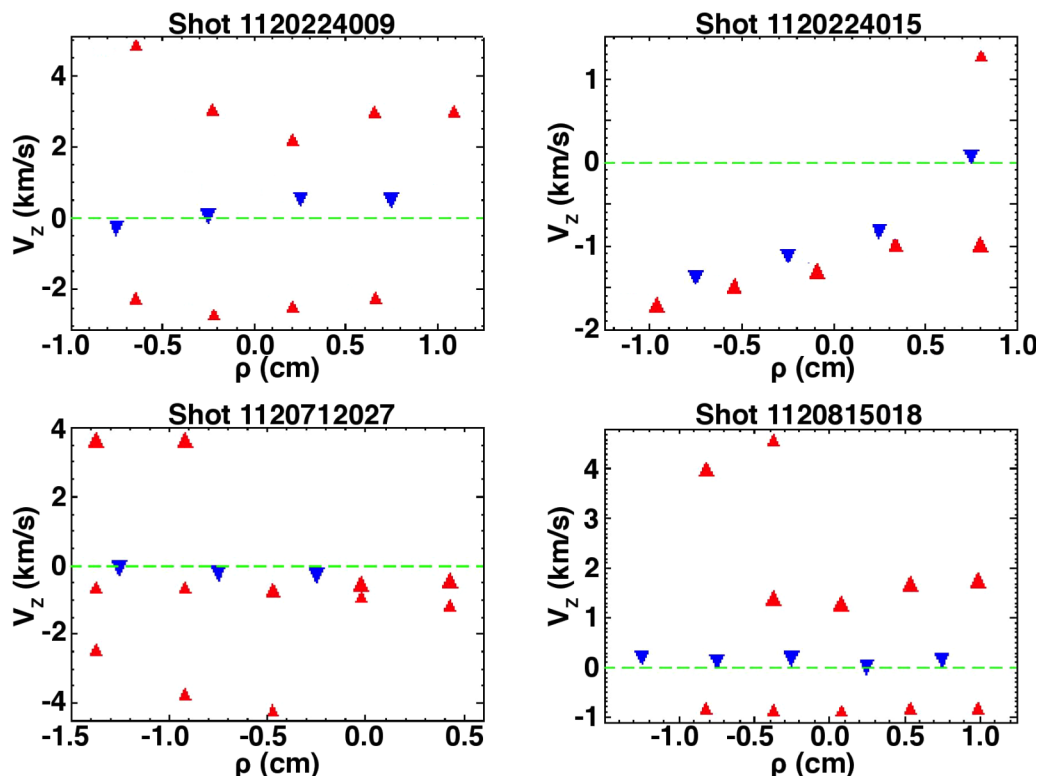


FIG. 2. Poloidal velocity measurements (km/s) for four Alcator C-Mod shots, using direct FA (red triangles) and tracking TDE (blue inverted triangles) versus  $\rho$ , the distance from the separatrix. The direct FA method can output multiple velocity measurements for a single location as it separates each signal into Fourier components.

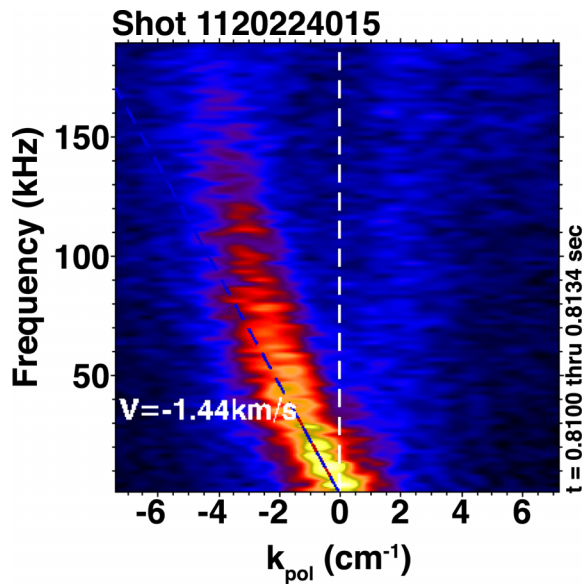


FIG. 3. Example of conditional spectrum from shot 1120224015 0.52 cm inside the separatrix with non-linear dispersion plotted as a function of frequency and wavenumber. The slope is not constant, indicative of nonlinear dispersion. The velocity measurement has been fitted to the peak in the Fourier spectrum at 30 kHz.

over a column of pixels, it tends to detect these counter-propagating features. The TDE analysis only measures velocity within a search box; very few of the counter-propagating features were localized enough to occur within a single search box. This will be discussed further below.

#### IV. SYNTHETIC GPI DIAGNOSTIC

In order to compare the tracking TDE and direct FA codes quantitatively, synthetic data must be used. By using synthetic

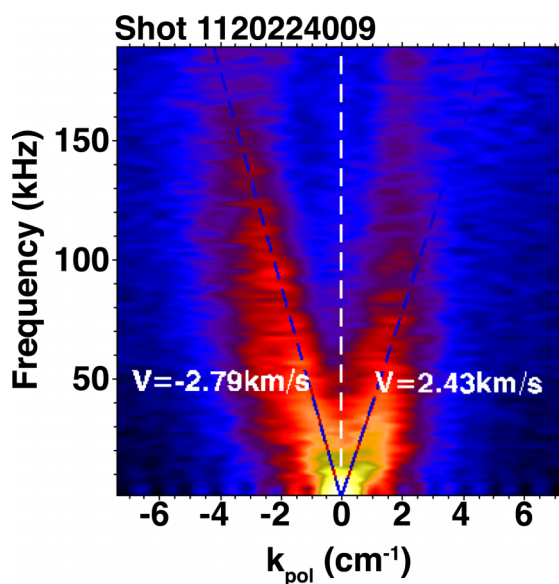


FIG. 4. Example of conditional spectrum with lobes in both negative wavenumber and positive wavenumber, 0.23 cm inside the separatrix. The Fourier method detected two different velocities:  $-2.79 \pm 0.42$  km/s and  $+2.43 \pm 0.36$  km/s, as indicated by the dashed lines. The tracking TDE method found 0.1 km/s as the velocity.

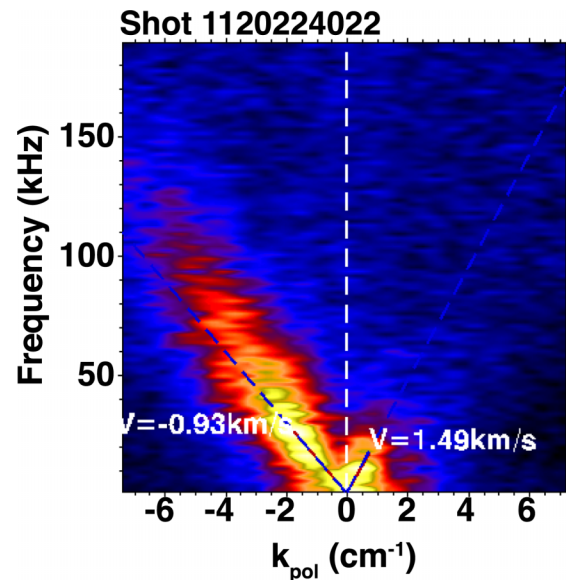


FIG. 5. Example of conditional spectrum with lobes in both negative wavenumber and positive wavenumber. Unlike Fig. 4, the peaks are not symmetric. The  $+k$  lobe only ranges from 0-30 kHz, while the  $-k$  lobe exists above 30 kHz. The velocity measurements were fitted to the peaks in the Fourier spectrum at 15 kHz for the  $+k$  lobe and 30 kHz for the  $-k$  lobe.

data, it is possible to systematically test for the strengths and weaknesses of the implementations of the direct FA and tracking TDE techniques (as described in Section II) for determining structure velocities. Without synthetic data, neither codes can be used to benchmark the other. For the synthetic data, the user will specify the velocity, size, distribution, and intensity of the structures (blobs), so that the accuracy and fidelity of each code and method is tested rigorously. This is to insight into the quantities that are “weighted” most heavily by each analysis technique with the ultimate goal of commenting on the appropriate use of each technique. In this section, we describe how the synthetic data are generated, compare the synthetic data to experimental data, and describe the results of applying both techniques to a simple synthetic case.

##### A. Generation of synthetic data

The basic assumption guiding the generation of synthetic blob data is that the emission structures detected are features with constant shape and velocity and have a distribution of sizes and intensities. The GPI system detects blob shapes that are in general elliptical.<sup>15</sup> For simplicity and to capture these observations, the user may specify synthetic blobs to be either circular or elliptical, and if elliptical, they may be rotated at some chosen angle from the R axis with some chosen elongation. For a given blob field, both a horizontal ( $V_R$ ) and vertical velocity ( $V_Z$ ) are defined. The code assumes frozen flow in the sense that all blobs in a single generated “blob field” will be moving with the same velocity at all times. However, it is noted below that different “blob fields” may be combined in a single time sequence. It is also constrained so that the blobs do not change shape or intensity as they move. The user-selected statistical distribution specifies which sizes and intensities are assigned to individual blobs in the field.

Currently, the options are a standard normal distribution and a standard gamma distribution (where gamma can be one up to nine in value),<sup>36</sup> where the gamma pdf is given by:

$$pdf = \frac{x^{\gamma-1} e^{-x}}{\Gamma(\gamma)}. \quad (4)$$

A maximum intensity and maximum full width at half of the intensity maximum (FWHM) for the blob distribution can then be defined. For elliptical blobs, the user can define the maximum semi-major axis length. Note that, as implemented, a given blob intensity and FWHM are determined by the same randomly generated value. Finally, a function governing how the intensity decays with distance from the center of a blob can be chosen, either a Gaussian shape or a Lorentzian shape.<sup>18,37</sup>

Three other important user options are the number of blob fields, where each field is a set of blobs with different input parameters, the number of time steps, and whether or not to add noise to the synthetic signal. First, the user may want to be able to have blobs moving at different speeds within the same time series of frames. The user can choose how many blob fields to generate, and the signals in each pixel or view will be added for each field generated. Thus, it is possible to generate several different fields with different velocities, distributions, and different intensities and sizes. Second, rather than fixing the length of time for which the signals will be generated, the length of time is variable set by the user. Third, the experimental data are subject to noise in the Phantom Camera. In order to include noise in the synthetic data, real system noise is taken from the C-Mod GPI data (from a shot that had no plasma) and is added to the synthetic signal. An example of the end result is shown in Fig. 6.

The time series of synthetic images is generated by creating features/blobs outside of the active analysis frame which then move into the field of view active frame after some number of time steps depending on the chosen velocity. Multiple fields with completely different characteristics can be combined into a single time series of frames. This method has the

disadvantage of limiting the maximum size of any generated blob, due to there being a finite amount of space outside the active frame in which the blobs are generated. In other words, there are only so many pixels outside the field of view active frame in which to create a blob.

## B. Comparison of synthetic data to experimental data

Because we wish to mimic the experimental data as much as possible, we provide user options for the shape (circular vs. elliptical), peak intensity distribution for a blob field (normal vs. gamma), and intensity distribution within a blob (Gaussian vs. Lorentzian). Furthermore, it is important to compare certain statistical properties of the synthetic data to those of the experimental data, namely, the probability density function (PDF). Examples of PDFs for both plasma data and a synthetic trial are given in Fig. 7, respectively. The synthetic data are specifically designed to output either a gamma or normal distribution of blob sizes and intensities. This is to mimic how blob intensity varies from being (approximately) normally distributed just outside the last closed flux surface to being gamma distributed (gamma = 9) in the far scrape off layer.<sup>36</sup> Since we are most concerned with the turbulence in the scrape off layer, for most trial runs, gamma = 9 is chosen. No strong dependence of the distribution on the velocity measurement has been found. Thus, to first order, we believe our synthetic data properly mimic the real data well enough to be used for this study.

## C. Sample analysis on single-velocity time series

The code has been designed to output a time series of image data with known characteristics. The synthetic data are designed to have uniform, isotropic fields of blobs all moving in the same direction at the same speed. To ensure that the code generated data properly, a test case is used, with the synthetic blobs moving straight upward in the images. In this instance,

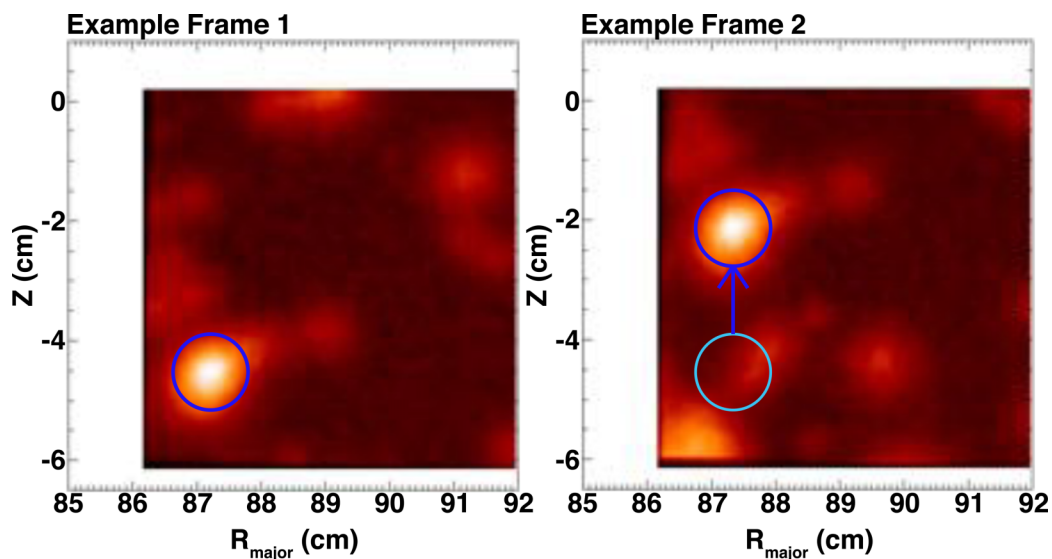


FIG. 6. Example of a circular synthetic blob field moving at constant velocity. The motion of a single blob is indicated by the arrow, with the original blob location circled in light blue and the new location circled in dark blue.

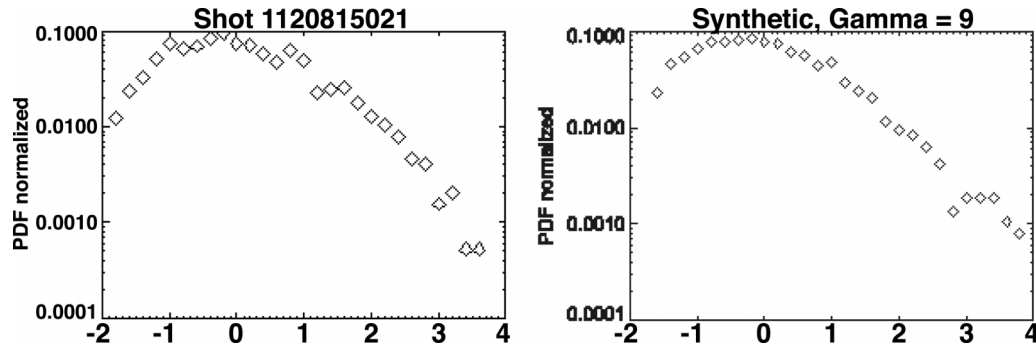


FIG. 7. Normalized (to total fluctuations in signal) PDF for a real shot (left) from a pixel viewing the far scrape-off-layer, and for a synthetic trial where  $\gamma = 9$  (right).

both the wavenumber-frequency spectrum and the conditional spectrum are expected to have a single lobe. The slope of the lobe is the measured velocity. This was indeed demonstrated for several trials (Fig. 8). Both the direct FA and tracking TDE analyses find the velocity to be 1 km/s to within 5%, for each radial location in the test frame.

Some limitations of the synthetic data include the fact that the synthetic blobs are static in time. They neither change shape, velocity, or intensity, nor do they merge with other blobs. These limitations are explained further in Section VII.

## V. APPLYING FA AND TRACKING TDE METHODS TO SYNTHETIC DATA

In this section, we describe results of applying the FA and tracking TDE methods to synthetic data. Limitations of each method are described.

### A. Fourier technique

Clear disagreements between the FA and the tracking TDE methods, when applied to experimental data, occur when

there are multiple lobes in the conditional spectrum (see Figs. 4 and 5) and when there is a single lobe, with a non-constant slope, i.e., nonlinear dispersion as shown in Fig. 3. In the case of multiple lobes, the FA method allows the measurement of multiple velocities, one velocity for each lobe. A major strength of the Fourier conditional spectrum technique is that it provides a wavenumber-frequency spectrum from which multiple feature velocities can be detected, which as mentioned above, can occur within columns of pixels.

Another strength of the FA method is that when non-linear dispersion is present, a velocity measurement can still be made by either taking the phase velocity at a fixed wavenumber or by fitting the Fourier peaks with a smooth curve and taking the derivative to find the group velocity as a function of wavenumber.

Despite these strengths in handling data sets with multiple velocities or with nonlinear dispersion, the FA method has major weaknesses. In the code under consideration, the poloidal velocity is overestimated if there is a significant radial velocity component. To demonstrate this with synthetic data, we generated a series of synthetic data sets, varying the ratio of the input  $V_Z$  to input  $V_R$ , and analyzed those shots with the

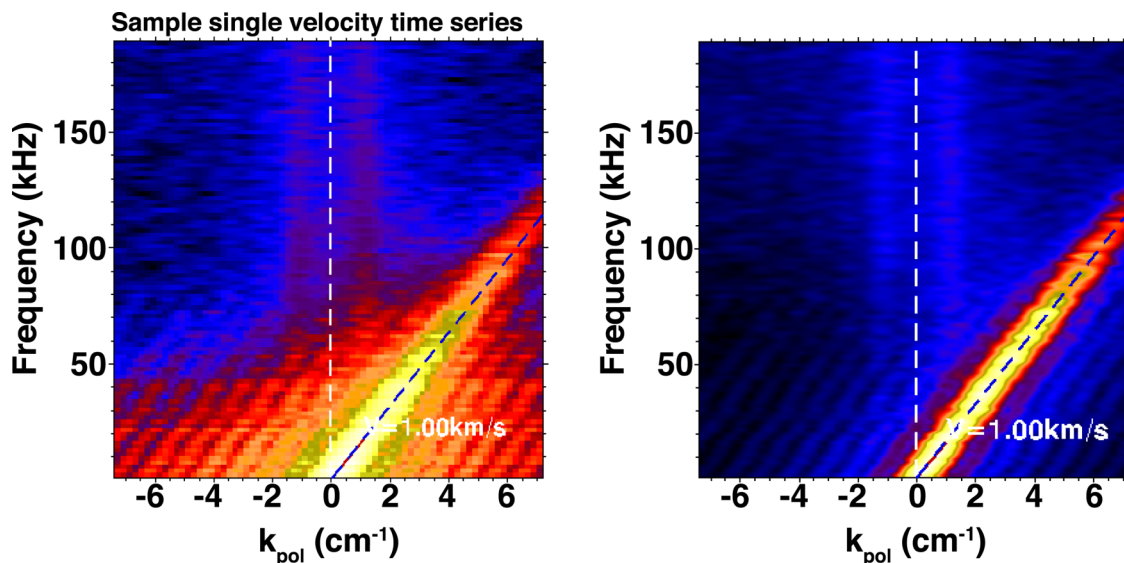


FIG. 8. (left) Spectrogram of the log of the spectral power (Fourier amplitude squared) as a function of poloidal wavenumber and frequency for a single-velocity field. (right) Conditional spectrum for the same single-velocity field. Input  $V_Z = 1.01$  km/s and input  $V_R = 0.0$  km/s. The red line through the lobe of the conditional spectrum indicates a phase velocity of 1.0 km/s, i.e., it reproduces the input vertical velocity. The errors in the measurements are  $\sim 4\%$ , by computing the least squares error from fitting to the peaks in the conditional spectrum.



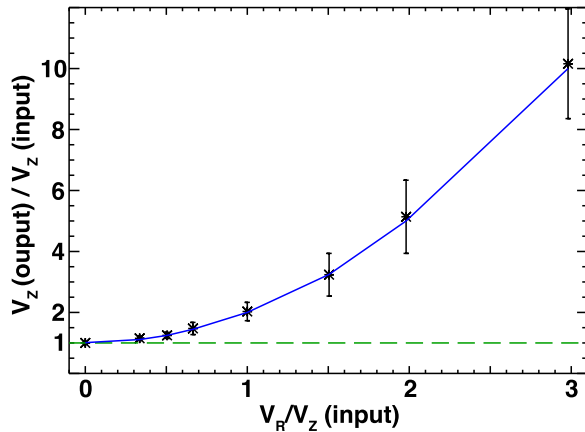


FIG. 9. Ratio of output to input vertical velocity vs. ratio of input horizontal to input vertical velocity for a series of synthetic shots. The green dashed line indicates what the output should have been based on the input velocities. The blue line represents the polynomial fit in (5).

Fourier implementation. The ratio of the output  $V_Z$  to input  $V_Z$  increases with increasing ratio of  $V_{Z,input}$  to  $V_{R,input}$  (Figure 9). This result is due to the fact that the Fourier analysis performs the spatial transform only in the vertical direction and not also in the radial dimension. In other words, this particular Fourier analysis transforms from the time domain into the frequency  $f$  domain, and also in the spatial domain to produce wavenumber  $k_Z$ , but not wavenumber  $k_R$ . In principle, if  $V_{R,output}$  can be measured, then this can be corrected assuming the blobs are wavefronts and therefore have different wavelengths in the R- and Z-directions,

$$V_Z(input) = \frac{V_Z(output)}{1 + \left(\frac{V_Z(output)}{V_R(output)}\right)^2}, \quad (5)$$

$$V_R(input) = \frac{V_R(output)}{1 + \left(\frac{V_R(output)}{V_Z(output)}\right)^2}. \quad (6)$$

Equation (5) is plotted as the blue curve in Figure 9; the data points are consistent with the curve and with Equation (5). In practice, this can be difficult to accomplish. As mentioned above, the FA code considered in this paper does not transform in R because that would involve transforming in two disparate regions of the plasma, which leads to significant error in the radial velocity that is evaluated. This can be mitigated somewhat by only taking a radial transform on signals from the SOL outside the separatrix. This also leads to issues in the sense that if the separatrix is too close to the edge of the frame, there will not be enough spatial points over which to perform the radial transform, without significant error in the measurement.

We emphasize that this is not the case for all FA implementations, and in cases where both directions can be transformed without any adverse effects on the results, this will be a strength of the general FA technique.

Another issue with this FA method is that it is subject to the well-known barber pole effect.<sup>16,38</sup> This occurs when the blobs are elliptical and not circular, and are moving at least somewhat radially. Shape does not affect measurements when the blobs move only vertically. To produce this effect using synthetic data, we generated two sets of synthetic data

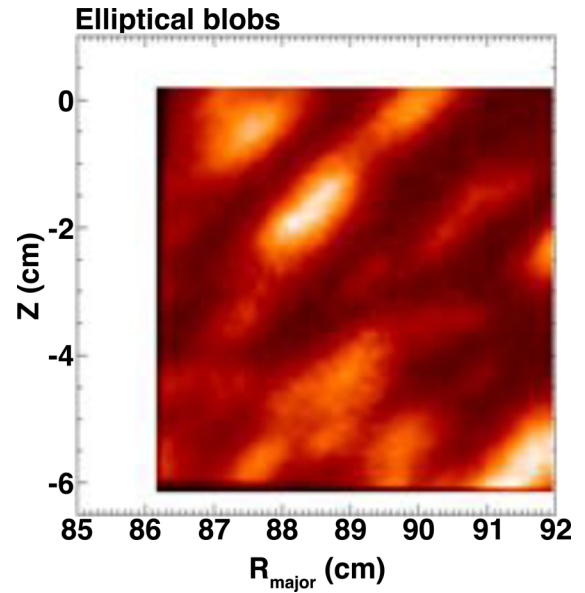


FIG. 10. Example frame showing elliptically shaped blobs, oriented so that their semi-major axes are tilted 45° above horizontal.

using elliptically shaped blobs. In both sets, the blobs are oriented so that the major axes of the ellipses are oriented in the direction of motion, and both sets of blobs were given the same maximum intensity and size (Fig. 10). However, in one set the blobs are moving at  $V_Z = 1$  km/s and  $V_R = 1$  km/s, and in the other set they are moving at  $V_Z = 0$  km/s and  $V_R = 1$  km/s. The poloidal FA was applied to each. In the former case, the wavenumber widths of the lobe significantly increases; in the latter case, not only is the width increased, but the lobes now occur with negative wavenumbers as if the blobs moved somewhat downward instead of only radially (Fig. 11). This is because the top parts of the ellipses are moving across the vertical bands over which the Fourier transforms are taken, before the lower parts of the ellipses (Fig. 10).

As described above, the shape of the blobs as viewed by the Phantom camera tend to be circular, while those as viewed by the APDs tend to be more elliptical. Since the experimental data are primarily from the Phantom camera, the barber pole effect likely does not have a significant impact on the results of the FA unless there is significant shear in the scrape-off-layer.

## B. Tracking TDE technique

As discussed in Subsection V A, the FA method is subject to the barber pole effect. It is already well-known that the barber pole effect is seen in ordinary TDE methods.<sup>39</sup> However, the tracking TDE method used in this work is not subject to this problem, as can be shown using synthetic data. The tracking TDE method essentially recovered the correct velocities in both elliptical blob cases:  $V_Z = 0.91$  km/s and  $V_R = 1.04$  km/s for the former case, and  $V_Z = -0.02$  km/s and  $V_R = 1.00$  km/s. As shown above (Fig. 11) for elliptical blobs, while the direct FA implementation outputted incorrect velocity measurements when the blobs were tilted at 45°, the tracking TDE technique found the correct velocities in both the poloidal and radial directions.

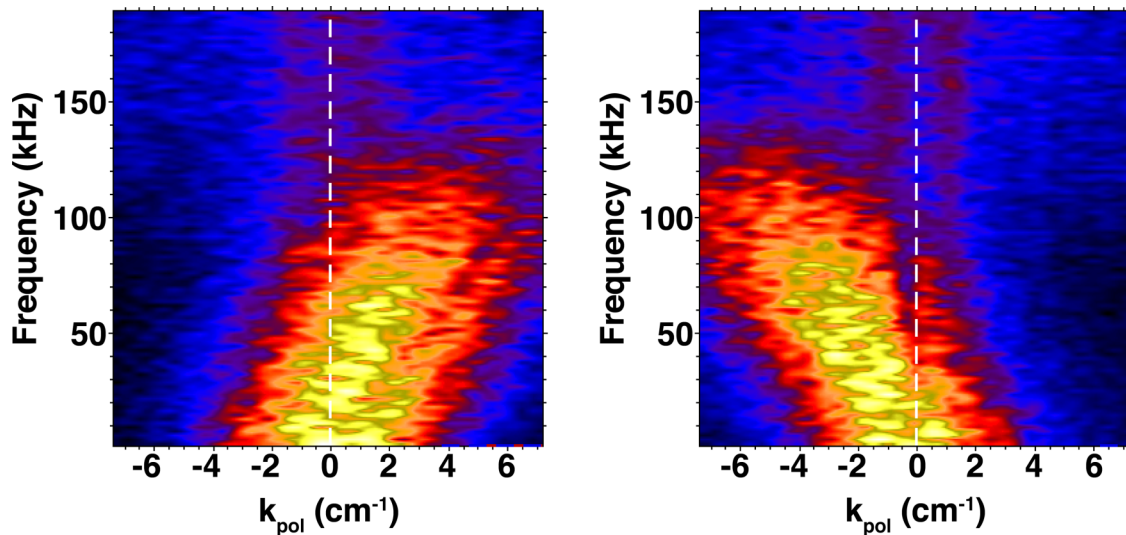


FIG. 11. Conditional spectra for synthetic data with elliptical blobs. (left) Blobs are moving at +1 km/s both poloidally and radially. (right) Blobs are moving in the positive radial direction at 1 km/s.

The reasons why this particular implementation of tracking TDE does not suffer from distortion due to blob shape is first, because the images have been smoothed, and second, that the cross correlation function is computed between a reference pixel and every pixel in a search box rather than only the pixels in the same column and row. Fedorczak *et al.* suggest using the pixels in the corners of a box surrounding the center pixel of a blob to obtain the shaping parameters.<sup>39</sup> The search box used in the tracking TDE method essentially takes the place of this.

As demonstrated also by these synthetic cases, the tracking TDE method is not affected by the disparate behavior inside and outside the separatrix for computing the radial velocity. It merely finds correlated motion within a search box for each pixel. This means that it can find the radial velocity independent of the poloidal velocity, and one measurement does not affect the other. This is an especially important strength since the blob structures have, in many cases, significant radial motion.

A major weakness of the tracking TDE method is that it relies on cross correlations, which as discussed above, are largest for the most intense features. Features which are not bright and moving at different speeds or in different directions from the most intense features will not be detected. This issue will be inherent in all TDE methods, not just the one presented here, unless the frequency range is restricted through the use of wavelets or digital filters. The effects of relying on cross correlations can be seen in Section III, where the examples had non-linear dispersion and multiple components with opposite signs in wavenumbers. In the former case, because the lower wavenumber components are typically brighter, unfiltered TDE methods will only find those brighter features. Again, this has been rectified in other implementations by filtering the time signals for different frequency bands. In the latter case for some shots, TDE methods will find an “average” velocity between the multiple components, or pick out which one is brighter. Applying filters will generally not improve the TDE methods’ performance in this latter case because the Fourier spectrum can have more than one value for the

same frequency with different wavenumbers. For other shots, if multiple components with opposite signs do not occur within the same search box, there is no effect on the TDE velocity measurements, as mentioned above for Figs. 4 and 5.

Another weakness is that the search box size can limit the detection of fast moving blobs as mentioned before, and also of large blobs. To illustrate this, the tracking TDE code was modified to test out different sizes of search boxes for synthetic data sets. In each case if the blobs were the size of the search box or larger, the code fails to output a measurement. For example, the code failed to output an answer when the search box size was  $11 \times 11$  pixels (roughly 1 cm by 1 cm) and the average FWHM of the blobs was set to be 1 cm.

## VI. MULTIPLE VELOCITY MEASUREMENTS AND SIZE SCALES

As discussed above, very often the experimental GPI data feature multiple lobes in the conditional spectra (see Figs. 4 and 5), or single lobes with a non-constant slope (i.e., nonlinear dispersion as shown in Fig. 3). Using the synthetic data, it is possible to show how such features are generated in the plasma. We can first generate synthetic data with multiple blob fields moving at different speeds. Fig. 12 shows a synthetic multiple-peak conditional spectrum (“Test Case 1”). There are three separate fields. Input velocities are:  $V_Z = -1.95, -1.29,$  and  $+0.78$  km/s;  $V_R = 0.39$  for all three fields. The tracking TDE code found  $-0.1$  km/s for the poloidal velocity.

While we are able to generate and mimic multiple peaks in the conditional spectra by using multiple blob fields, this does not necessarily indicate that multiple fields of blobs are causing this behavior in the experimental data for every shot. Experimentally, we expect that blobs moving in opposite directions within the same field of view will arise only when there is sharp  $E \times B$  velocity gradient within the field of view. Cases such as Fig. 5 in which there are two lobes, indicative of phase velocities of roughly the same magnitude, but different signs

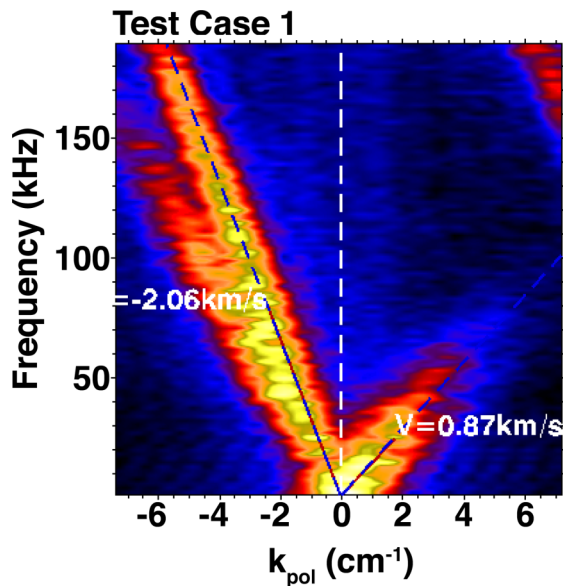


FIG. 12. Conditional spectra for synthetic data with three fields, “Test Case 1.” The velocity measurement for the top left lobe was fitted to the peak in the Fourier spectrum at 100 kHz, while the velocity for the right lobe was fitted for the peak at 30 kHz. The measurements are consistent with what is expected from plugging the input poloidal and radial velocities into Equations (5) and (6).

could be a combination of  $E \times B$  motion for one lobe and wave-like fluctuations for the other, as seen previously<sup>29</sup> for L-mode plasmas. However, reviewing the set of C-Mod shots in Zweben *et al.*,<sup>19</sup> these conditional spectra were most often seen in ELMy H-Modes,<sup>15</sup> and there did appear to be counter-propagating features within column of pixels analyzed with the Fourier method. Furthermore, this does not explain situations in which there are multiple lobes in the Fourier spectrum with the same sign in phase velocity. For these instances, there are a few possible explanations: that there are multiple structures in the same field of view moving at different speeds (caused by velocity gradients), that there is an unknown diagnostic issue, and that for large, well-structured blobs, there is a large radial velocity component making part of the blobs appear to move in opposite directions.

The next issue considered for the synthetic data was the effect of different-sized blobs moving at different speeds. Fig. 13 shows “Test Case 2,” a synthetic data set with eight separate sets of blob fields was used with  $V_Z$  ranging from 0.5 km/s to 3.3 km/s and zero  $V_R$  for simplicity. The inputs are listed in Table I, with  $\gamma = 9$ . The option to allow different sets of blobs to have different sizes which would be static throughout the simulation, e.g., one set might have blobs that range from 0–0.3 cm in radius and another set could have blobs that range from 0.3–0.4 cm, was used to create this set. For Fig. 13, the slower-moving blobs were chosen to be smaller than the faster-moving ones. As can be seen, there is a gradual change in the slope of the dispersion relation. The tracking TDE code found the poloidal velocity to be 1.7 km/s and the radial velocity to be 0.07 km/s, while the direct FA code found poloidal velocity of  $1.7 \pm 0.4$  km/s, with clear evidence that there are other velocities present, leading to the appearance of a nonlinear dispersion similar to that found in the experimental data in

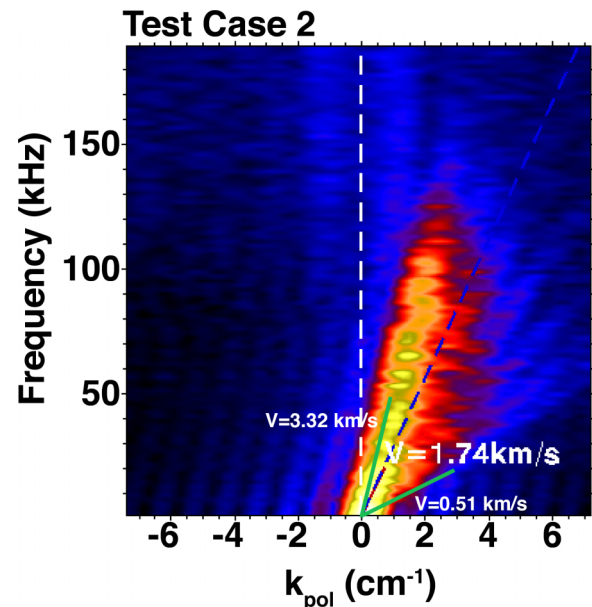


FIG. 13. Conditional spectrum for synthetic “Test Case 2,” giving non-linear dispersion with a gradual change in slope. Inputs are included in Table I. The velocity was fitted to the peak in the Fourier spectrum at 30 kHz. The lowest and highest input velocities are shown in green and labeled.

Fig. 3. The velocity obtained is between the minimum and maximum input values.

A third set of synthetic data, “Test Case 3,” was generated (Fig. 14) to produce a sudden change in the slope, as opposed to a gradual change. Inputs are listed in Table II, with  $\gamma = 9$  and  $V_R = 0$ . Note that in this case, the larger blobs are now moving slower than the smaller ones. For larger  $k$ , the slope is constant. The tracking TDE code found  $V_Z$  to be 1 km/s, and  $V_R$  to be 0.06 km/s. The FA code found  $V_Z$  to be  $0.8 \pm 0.15$  km/s, which is consistent with the smaller-velocity, lower-frequency inputs. In this case, the inputs were chosen so that the high- $f$ , high- $k$  part of the conditional spectrum would appear not to extrapolate back to the origin. This produces a break in slope at a frequency of approximately 20 kHz.

Since we have demonstrated that we can generate data that result in conditional spectra that appear to have nonlinear dispersion, we can now explore what causes this nonlinear dispersion in the experimental data. We first consider blob size. Little has been mentioned in the literature about scalings of blob poloidal velocity with blob size. Theory predicts that for

TABLE I. Input values for synthetic Test Case 2, which show changes in slope due to different-sized blobs moving at different speeds. Velocities are given in km/s, size in cm, and intensity in arbitrary units.

$V_Z$ (km/s)	Intensity range	Size range (cm)
0.51	0.00–1.83	0.0–0.23
0.63	1.42–2.01	0.23–0.32
0.82	1.94–2.51	0.32–0.41
1.13	2.27–2.58	0.41–0.47
1.52	2.31–3.14	0.47–0.64
2.03	2.76–3.32	0.64–0.77
2.62	2.87–3.29	0.77–0.88
3.32	2.77–5.33	0.88–1.7



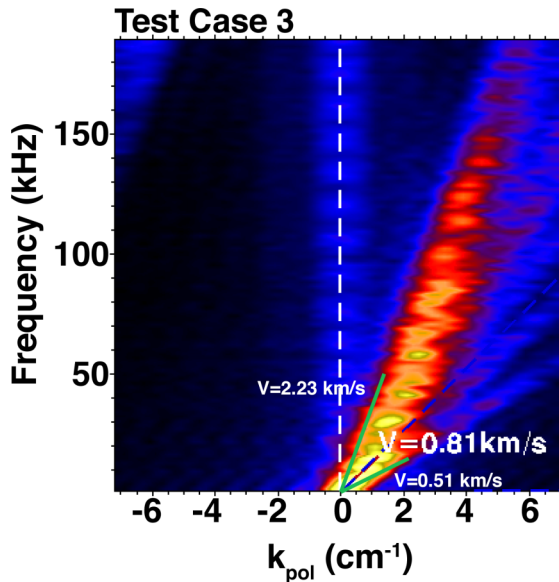


FIG. 14. Conditional spectrum for synthetic “Test Case 3,” non-linear dispersion with a break in slope. Inputs are included in Table II. The velocity in this case was fitted to peak in the Fourier spectrum at 20 kHz, approximately where the break in slope is located.

most cases the radial velocity decreases with blob size.<sup>2,40</sup> This would imply that smaller blobs would have larger radial velocities and hence could have artificially large poloidal velocities when measured with direct Fourier methods such as the one presented and not correcting for waveform effect. Another recent paper<sup>41</sup> reported using 1D velocimetry techniques to determine that for an L-Mode shot on ASDEX-Upgrade, the poloidal velocity increased with increasing blob size when the blobs were at least 1.5 cm in radius while there was little relationship between blob size and radial velocity.

So far, we have demonstrated that the conditional spectra alone cannot discern the relationship between blob size and blob velocity. Thus, we now consider the power spectra associated with these synthetic data sets in comparison to those of two experimental discharges which we attempted to mimic.

Keeping in mind that the power spectrum should not be affected by the sign of the phase velocity, we first compare the power spectra of the gradually changing slopes, both experimental and the synthetic “Test Case 2” (Figs. 3 and 13, respectively). As can be shown in Fig. 15, the synthetic power spectrum does not mimic the experimental one, neither in shape nor in magnitude.

TABLE II. Input values for “Test Case 3.” Gamma = 9 and  $V_R = 0$ .

$V_Z$ (km/s)	Intensity range	Size range (cm)
0.51	0.94–4.00	0.33–1.42
0.74	1.00–2.89	0.33–0.94
0.98	1.13–1.67	0.32–0.47
1.17	1.33–2.00	0.28–0.43
1.36	1.44–2.31	0.24–0.38
1.68	1.38–2.41	0.19–0.33
1.95	1.07–2.13	0.14–0.28
2.23	0.004–1.83	0.001–0.24

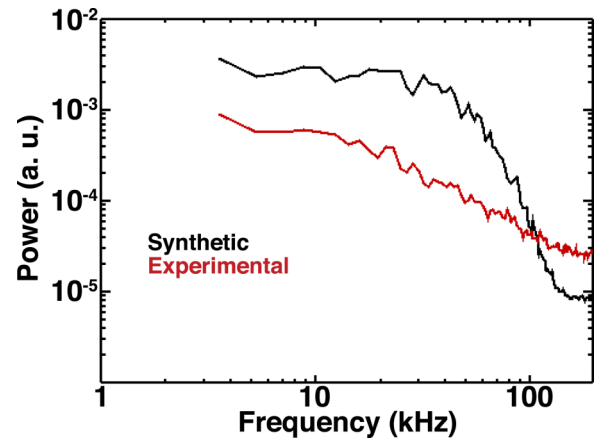


FIG. 15. Power spectra of synthetic test case 2 in which larger blobs move faster and experimental shot 1120224015 (Fig. 3). Neither shape nor magnitude match.

Next we compare the power spectra (in Fig. 16) for the synthetic “Test Case 3” (whose conditional spectrum is shown in Fig. 14), and its companion experimental discharge (whose conditional spectrum is shown in Fig. 17). Both the slope at frequencies greater than 20 kHz, and the magnitude are in better agreement, which tends to indicate that the smaller blobs move faster than the larger ones in the experimental data. In other words, blob velocity appears to decrease with blob size in instances where there is nonlinear dispersion present.

However, the parameters chosen for these test cases led to conditional spectra with different behavior in the lobes’ slopes. To demonstrate that the selected blob size-velocity relationship was correct, we have generated a synthetic “Test Case 4” (Fig. 18) to produce a gradual change in slope, but with the larger blobs are moving slower than the smaller ones. Inputs are listed in Table III, with gamma = 9 and  $V_R = 0$ . The qualitative result is the same after modifying the input intensities. Note that in all of these cases, the radial velocity was zero. These effects are created with input poloidal velocities only. The tracking TDE code found the poloidal velocity to be 1.02 km/s and the radial velocity to be 0.06 km/s. The reduction

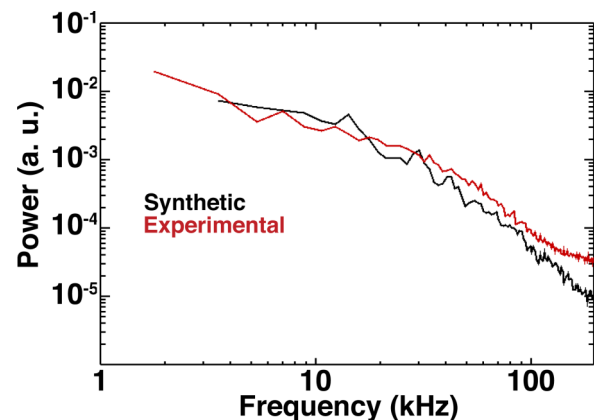


FIG. 16. Power spectra of synthetic test case 3 in which larger blobs move faster and experimental shot 1120224009 (Fig. 17).



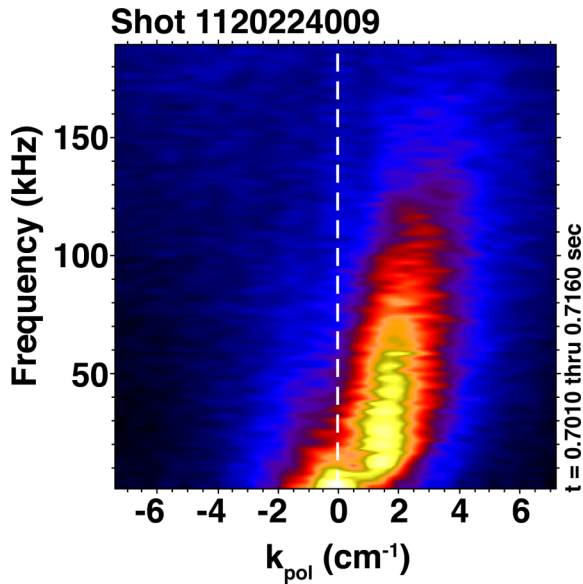


FIG. 17. Conditional spectrum for C-Mod shot 1120224009, 1.11 cm outside the separatrix, which shows a break in slope, and is the experimental companion shot for synthetic test case 4.

in velocity from that of the previous shot is due to changes in intensities.

We now compare the power spectrum (Fig. 19) of this shot to the experimental discharge shown in Fig. 17. We also include in Fig. 19 one final synthetic case (shown in green) is very similar to and based on “Test Case 3,” but with radial velocity components equal to one half those of the poloidal velocity components, such that the final predicted poloidal velocities would be those given in Table II, as calculated with the wavefront equations presented in Sec. V. We note that all but “Test Case 2” give approximately the same slope in the power spectrum as the experimental discharge.

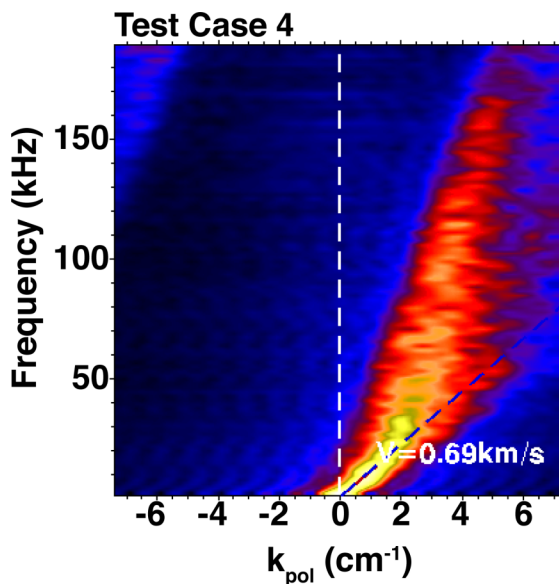


FIG. 18. Conditional spectrum for non-linear dispersion with a gradual change in slope, “Test Case 4.” This is a similar data set to test shot 111161206, except for a reversal in the relationship of blob size and blob velocity. Inputs are included in Table III. The velocity was fitted to the peak in the Fourier spectrum at 20 kHz.

TABLE III. Input values for “Test Case 4,”  $\Gamma = 9$  and  $V_R = 0$ .

$V_Z$ (km/s)	Intensity range (cm)	Size range (cm)
0.51	1.44–3.33	0.61–1.42
0.63	1.44–2.89	0.47–0.94
0.74	1.16–2.17	0.38–0.71
0.90	1.20–2.40	0.28–0.57
1.06	0.93–2.33	0.19–0.47
1.25	0.49–1.71	0.09–0.33
1.45	0.38–1.66	0.07–0.31
1.68	0.28–1.67	0.05–0.28
1.92	0.14–1.59	0.02–0.25
2.19	0.003–1.50	0.0005–0.24

This gives confidence that the blobs detected in the experimental data are in fact increasing in speed with decreasing size.

To discern if this is a real effect or an artificial effect from having radial velocity components, movies were generated of the Phantom-based data for the experimental discharges considered. The movies for C-Mod shot 1120224015, representative of the gradually changing slope in Fig. 3, show some significant radial motion. The movies for shot 1120224009, representative of the break-in-slope case, still showed some radial motion though not as much. This indicates that some of the poloidal velocity results obtained here could be spurious due to having actual radial motion.

## VII. DISCUSSION, CAVEATS, AND FUTURE WORK

### A. Remaining issues with synthetic GPI data generation

The results and conclusions of this work rely heavily on the use of synthetic GPI data. While these were designed to imitate the real data as much as possible, there are limitations on the technique’s capabilities. Here, caveats regarding the synthetic diagnostic itself are discussed and will be addressed further in future work.

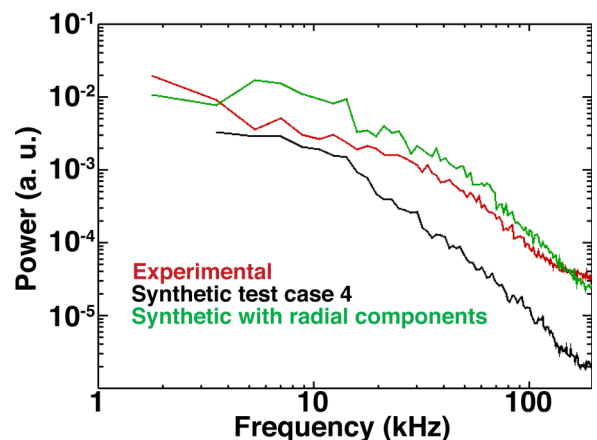


FIG. 19. Power spectra of synthetic “Test Case 4,” a synthetic set similar to “Test Case 3” but with finite radial components, and experimental shot 1120224009 (Fig. 17). The slopes and magnitudes better fit the experimental data.

First, the velocity and direction of an individual blob does not change in time. In the real data, blobs can be seen changing direction and speed depending on their location. Implementing this in the synthetic diagnostic would enable, for example, confirming that oscillations are causing the instances of multiple peaks with opposite signs in phase velocity. While it is possible to modify the synthetic diagnostic to have individual blobs to change speeds and directions, we leave this as future work.

The second major limitation is that the individual blobs in the synthetic data do not change intensity in time or grow in size. In the experimental data, as the blobs move radially, they change in intensity. This behavior would affect velocity measurements made with any TDE or optical flow technique, but the specific qualitative and quantitative effects depend on what specific changes occur. Improving the diagnostic to include these effects in the future would also allow for similar testing of time-dependent analysis codes and methods.

A third limitation is that the synthetic data generation routine does not currently allow the user to input an equation governing dispersion in the conditional spectra. In other words, the synthetic data can be specified only with a range of blob sizes assigned to a certain constant velocity, forming a step function of velocity versus size. Smoothing out this function by modifying the diagnostic to assign a unique velocity to each unique blob size may resolve some of the issues presented in Sec. VI.

A fourth limitation is that while instances in which the Alcator C-Mod shots presented in Section III have been mimicked with the synthetic data sets in Section VI, this does not imply that these are unique. Both the Fourier method and the hybrid tracking TDE technique are subject to loss of information when analyzing data.

## B. Remaining issues with the analysis techniques of experimental and synthetic data

One major caveat is that while this paper examined different velocimetry techniques, the results of the paper are limited to the examination of individual implementations, rather than the techniques in general. So while the conclusions are true for the specific implementations of FA<sup>15</sup> and tracking TDE<sup>19</sup> methods that have led to the discrepancies described here, they may not be true for others. It is certainly important to consider each issue raised when choosing a technique, and to examine a particular code to ensure that any issues are mitigated. *The best possible way to ensure accurate results is to use multiple techniques to analyze the same experimental data and search for general agreement.* For example, starting with direct Fourier methods could immediately reveal the presence of dispersion, multiple Fourier peaks, or a widened peak indicative of radial motion. A TDE or other method could then be used with the caveat that a filter might need to be applied to select only certain frequencies, especially if dispersion is detected. Alternatively, starting with the tracking TDE to find the radial velocity could reveal whether or not results from a direct Fourier method will be valid for the poloidal velocities. The tracking TDE analysis could be repeated for different frequency ranges if there is any indication that the blobs are not all moving at the same speed.

A second caveat is that while optical flow and orthogonal dynamic programming techniques are gaining in popularity,<sup>16,28</sup> we have not formally considered them here. Use of these techniques could shed some more light on, for example, how blob velocity scales with velocity and shape. We have also not, in this work, considered how to adapt either implementation of the direct Fourier method and TDE method for time-dependent analysis. We leave as future work to complete a formal comparison of the methods here with an optical flow technique and to consider time-dependent analysis.

A third major caveat is that any issues between velocimetry methods can be exacerbated by differences in the type of detection, e.g., differences between Camera-based and APD-based GPI data. Note that for this work, only Phantom-based GPI data were used. Nevertheless, some analysis methods are designed to be used with certain detectors. The tracking TDE method, for example, is most suited for use with the Phantom Camera. When using multiple analysis techniques on the same data, each technique applied must be well-suited for analysis of data from the detector used.

## C. Remaining issues with analysis results and implications for experimental data

This paper has not gone into great detail about the physical explanations for what is causing the nonlinear dispersion and multiple-velocity spectra, even though these features can be replicated with the synthetic data very effectively. We first summarize what has been stated above and then offer more insights into future investigation.

For the multi-velocity spectra such as the one in Fig. 5, there are several possible explanations. One is that each lobe might be caused by different phenomena, e.g., wave-like fluctuations versus  $E \times B$  motion. Other instances include viewing regions with sharp velocity gradients, or having radial motion such that the front of a circular or elliptical blob appears to be moving vertically upward and downward as it moves across the field of view.

For this spectra that have nonlinear dispersion (different-sized blobs move at different speeds), there are a few possibilities. First, larger-sized blobs might sample a variety of electric fields if the  $E \times B$  shear is large enough and thus yield only a skewed representation of the local  $E \times B$  velocity, while smaller blobs do not. This might explain why the magnitude of the gradient in the slopes of the conditional spectra decrease with increasing wavenumber. In other words, the nonlinearity in the dispersion tends to occur at lower frequencies and smaller wavenumbers.

## VIII. CONCLUSIONS

This paper addressed discrepancies between published plasma edge and SOL turbulence structure velocities measured with a tracking TDE method<sup>19</sup> and those measured with a direct FA method<sup>15</sup> from the same GPI data. The main sources of the discrepancies come from two general effects: first, evidence of turbulent blob structures moving at different speeds depending on their size, and second, blob structures appear to move in opposite directions within the same field of

view. To address this issue, understand the reasons for these discrepancies, and to improve the usage of these velocimetry methods, a synthetic GPI diagnostic was developed that is used to generate synthetic data sets where blobs move at user-defined velocities through the appropriate field of view. These synthetic blobs have user-defined intensities, sizes, and distributions.

Several synthetic data sets were generated with the synthetic diagnostic, which revealed that the direct Fourier method considered here was subject to the barber pole effect while the tracking TDE was not. The synthetic data also revealed that the direct Fourier technique, as currently implemented, measures poloidal velocities which are incorrectly too large when there is a significant radial component and that it is, as suspected, subject to the barber pole issue. The synthetic data also uncovered a couple of issues with the tracking TDE, namely, that without frequency band filtering, it weighs the brightest features too heavily and that the size of the search box needs to be larger than the largest blobs in the field of view to obtain an accurate measurement.

With appropriate choice of input parameters, one can generate synthetic data that mimic the situations in which the poloidal velocity obtained with direct Fourier method disagreed with that of the tracking TDE. Some explanations for this were presented, including a consideration of how blob velocity varies with blob size. Several outstanding issues regarding the diagnostic and analysis are presented, which we leave as future work to address.

## ACKNOWLEDGMENTS

The authors thank the anonymous referees for comments which improved the paper. Experimental work on Alcator C-Mod is supported by US DOE Agreement No. DE-FC02-99ER54512. J.M.S. is supported by the National Science Foundation Graduate Research Fellowship Program, under Grant No. 1122374.

- <sup>1</sup>X. Garbet *et al.*, *Phys. Rev. Lett.* **91**, 035001 (2003).
- <sup>2</sup>D. A. D'Ippolito, J. R. Myra, and S. J. Zweben, *Phys. Plasmas* **18**, 060501 (2011).
- <sup>3</sup>S. J. Zweben *et al.*, *Phys. Plasmas* **9**, 1981 (2002).
- <sup>4</sup>S. J. Zweben, *Phys. Fluids* **28**, 974 (1985).
- <sup>5</sup>D. A. D'Ippolito, J. R. Myra, and S. I. Krasheninnikov, *Phys. Plasmas* **9**, 222 (2002).
- <sup>6</sup>J. A. Boedo *et al.*, *Phys. Plasmas* **21**, 042309 (2014).
- <sup>7</sup>N. Yan *et al.*, *Plasma Phys. Controlled Fusion* **55**, 115007 (2013).
- <sup>8</sup>M. Willensdorfer *et al.*, *Plasma Phys. Controlled Fusion* **56**, 025008 (2014).
- <sup>9</sup>G. McKee *et al.*, *Rev. Sci. Instrum.* **70**, 913 (1999).
- <sup>10</sup>R. J. Maqueda *et al.*, *Rev. Sci. Instrum.* **72**, 931 (2001).
- <sup>11</sup>J. L. Terry *et al.*, *Phys. Plasmas* **10**, 1739 (2003).
- <sup>12</sup>S. J. Zweben *et al.*, *Nucl. Fusion* **44**, 134 (2004).
- <sup>13</sup>S. C. Liu *et al.*, *Rev. Sci. Instrum.* **83**, 123506 (2012).
- <sup>14</sup>I. Shesterikov *et al.*, *Rev. Sci. Instrum.* **84**, 053501 (2013).
- <sup>15</sup>I. Cziegler, "Turbulence and transport phenomena in edge and scrape-off-layer plasmas," Ph.D. thesis, Massachusetts Institute of Technology, Cambridge, MA 2011.
- <sup>16</sup>T. Munsat and S. J. Zweben, *Rev. Sci. Instrum.* **77**, 103501 (2006).
- <sup>17</sup>L. M. Shao *et al.*, *Plasma Phys. Controlled Fusion* **55**, 105006 (2013).
- <sup>18</sup>J. R. Myra *et al.*, *Nucl. Fusion* **53**, 073013 (2013).
- <sup>19</sup>S. J. Zweben *et al.*, *Plasma Phys. Controlled Fusion* **55**, 072503 (2013).
- <sup>20</sup>R. Kube *et al.*, *J. Nucl. Mater.* **438**, S505 (2013).
- <sup>21</sup>S. J. Zweben *et al.*, *Plasma Phys. Controlled Fusion* **54**, 025008 (2012).
- <sup>22</sup>I. Cziegler *et al.*, *Phys. Plasmas* **20**, 055904 (2013).
- <sup>23</sup>I. Cziegler *et al.*, *Plasma Phys. Controlled Fusion* **56**, 075013 (2014).
- <sup>24</sup>H. Q. Wang *et al.*, *Phys. Rev. Lett.* **112**, 185004 (2014).
- <sup>25</sup>S. J. Zweben *et al.*, *Plasma Phys. Controlled Fusion* **56**, 095010 (2014).
- <sup>26</sup>I. Cziegler *et al.*, *Plasma Phys. Controlled Fusion* **54**, 105019 (2012).
- <sup>27</sup>Y. Sechrest *et al.*, *Phys. Plasmas* **18**, 012502 (2011).
- <sup>28</sup>G. M. Quenot, J. Pakleza, and T. A. Kowalewski, *Exp. Fluids* **25**, 177 (1998).
- <sup>29</sup>I. Cziegler *et al.*, *Phys. Plasmas* **17**, 056120 (2010).
- <sup>30</sup>J. M. Beall, Y. C. Kim, and E. J. Powers, *J. Appl. Phys.* **53**, 3933 (1982).
- <sup>31</sup>R. N. Bracewell, in *Fourier Analysis and Imaging* (Springer, New York, 2003), Chap. 6, p. 209.
- <sup>32</sup>M. Xu *et al.*, *Phys. Plasmas* **17**, 032311 (2010).
- <sup>33</sup>G. Jacovitti and G. Scarano, *IEEE Trans. Signal Process.* **41**, 525 (1993).
- <sup>34</sup>S. Zoletnik *et al.*, *Plasma Phys. Controlled Fusion* **54**, 065007 (2012).
- <sup>35</sup>M. Jakubowski *et al.*, *Rev. Sci. Instrum.* **72**, 996 (2001).
- <sup>36</sup>O. E. Garcia *et al.*, *J. Nucl. Mater.* **438**, S180 (2013).
- <sup>37</sup>J. E. Maggs and G. J. Morales, *Phys. Rev. Lett.* **107**, 185003 (2011).
- <sup>38</sup>Y. C. Ghim *et al.*, *Plasma Phys. Controlled Fusion* **54**, 095012 (2012).
- <sup>39</sup>N. Fedorczak *et al.*, *Phys. Plasmas* **19**, 122302 (2012).
- <sup>40</sup>S. I. Krasheninnikov, *Phys. Lett. A* **283**, 368 (2001).
- <sup>41</sup>T. Kobayashi *et al.*, *Rev. Sci. Instrum.* **85**, 083507 (2014).